# Fluid Flow Estimation Through Integration of Physical Flow Configurations

Christoph S. Garbe*

IWR, University of Heidelberg
Christoph.Garbe@iwr.uni-heidelberg.de

**Abstract.** The measurement of fluid flows is an emerging field for optical flow computation. In a number of such applications, a tracer is visualized with modern digital cameras. Due to the projective nature of the imaging process, the tracer is integrated across a velocity profile. In this contribution, a novel technique is presented that explicitly models brightness changes due to this integration. Only through this modeling is an accurate estimation of the flow velocities feasible. Apart from an accurate measurement of the fluid flow, also the underlying velocity profile can be reconstructed. Applications from shear flow, microfluidics and a biological applications are presented.

## 1 Introduction

Recently, modern techniques of motion estimation have made their arrival in the field of fluid dynamic measurements. Here, the main emphasis has been on regularizing the flow field, either by div-curl regularization [1] or by modeling the flow field based on physical constraints [2,3].

Apart from regularizing the flow field, brightness changes play an important role in a number of fluid dynamic applications. Often, due to transport phenomena the density of tracers change. The same holds true for temperature fields in the case of thermographic visualizations. An accurate modeling of these intensity changes based on the transport phenomena is fundamental to achieving accurate flow estimates. Moreover, apart from the flow field, additional information can be extracted from estimating parameters of brightness change models. These can be the air-water net heat flux from infrared image sequences of the air-water interface or chemical reactions from satellite remote sensing. These are important parameters in their own right.

For flow visualization, scalar quantities such as tracer particles or dyes are added to the flow. Also, heat can be used to visualize interfacial fluid flow. These scalars are visualized with digital or thermographic cameras, respectively. Due to the projective nature of the imaging process, the scalar concentration is integrated along the line of sight of the imaging optics. Depending on the flow configuration and the imaging set-up, frequently an integration across velocity

* The author acknowledges financial support by the DFG within the priority programs 1114 and 1147.

F.A. Hamprecht, C. Schnörr, and B. Jähne (Eds.): DAGM 2007, LNCS 4713, pp. 92–101, 2007.
© Springer-Verlag Berlin Heidelberg 2007

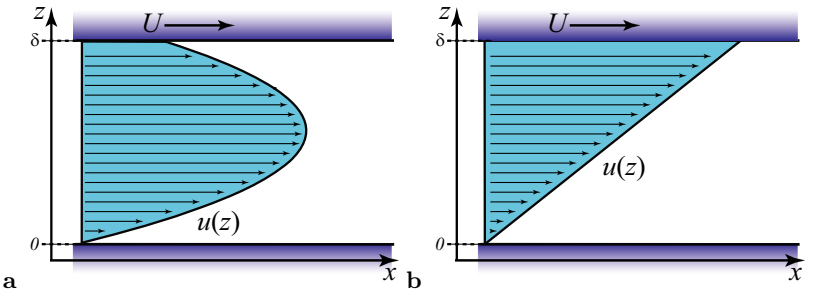


**Fig. 1.** Flow between parallel plates. The bottom plate is stationary, the upper one moving to the right at the velocity $U$. In **a** an additional pressure gradient $dp/dx < 0$ is driving the fluid, in **b** Plane Couette flow is shown ($dp/dx = 0$).

profiles has to be performed. In the case of parabolic flow profiles this process is also known as Taylor dispersion [4]. The visualized structures appear to diffuse anisotropically due to the integration. Very often, this unwanted effect cannot be circumvented experimentally. In this contribution, general motion models will be presented that explicitly model the projective process across flow profiles of different orders. This makes it feasible to accurately estimate the velocity and reconstruct the three dimensional flow profile at the same time.

Based on the novel motion models, the model parameters are estimated in a local extended structure tensor framework. If physically based regularization is of interest to the application, the presented framework can readily be incorporated into variational frameworks. However, this is not the topic of this contribution. The novel framework will be applied to shear flow configurations, microfluidics and biological applications.

## 2 Flow Profiles

### 2.1 Plane Couette Flow

The equation of motion for a flow of uniform density $\rho$ is given by the Navier-Stokes equation for an incompressible fluid [5]:

$$\frac{d\boldsymbol{u}}{dt} = \boldsymbol{g} - \frac{1}{\rho}\nabla p + \frac{\mu}{\rho}\nabla^2\boldsymbol{u} = -\frac{1}{\rho}\nabla p_d + \nu\nabla^2\boldsymbol{u}, \tag{1}$$

where $\mu$ is the viscosity and $\nu = \mu/\rho$ is the kinematic viscosity. $\boldsymbol{g}$ is the acceleration of gravity and $\nabla p$ is a pressure gradient incident on the fluid. $\boldsymbol{u}$ is the fluid velocity we are interested in. The dynamic pressure is given by $p_d = p - p_s$ and $\boldsymbol{g} = 1/\rho \cdot \nabla p_s$ results from the hydrostatic pressure for a fluid at rest.

Such a flow is generally driven by a combination of an externally imposed pressure gradient and the motion of the upper plate at uniform velocity $U$, as

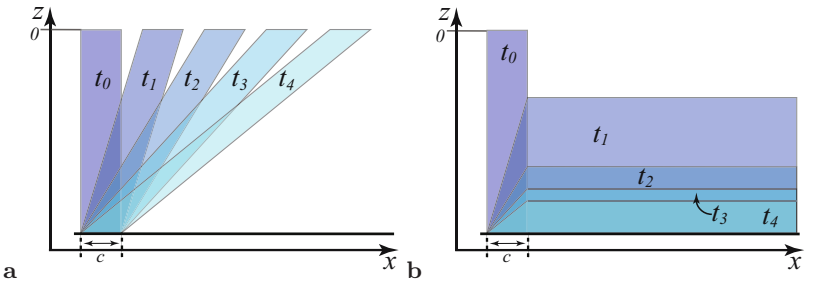


**Fig. 2.** Sketch of a marker in plane Couette Flow during time steps $t_1 - t_4$ in **a**. The marker is written at time $t_0$. It is sheared due to the flow. Shown in **b** is the depth integration of the marker, as visualized with the camera.

shown in Figure 1. The two plates are separated by the distance $\delta$. Applying the appropriate boundary conditions [5] this results in the equation

$$u(z) = \frac{z \cdot U}{\delta} - \frac{z}{2\mu}\frac{dp}{dx}(\delta - z)\,. \tag{2}$$

In the case of plane Couette flow, illustrated in Figure 1**b**, the flow is driven by the motion of the upper plate alone, without any externally imposed pressure gradient. For this case, Equations (2) reduces to

$$u(z) = \frac{z \cdot U}{\delta} \tag{3}$$

Plane Couette flow is a very good approximation for a number of shear driven flows. It can be used to describe the velocity structure at the wind driven sheared interface between atmosphere and ocean, particularly in the event of a surfactant covered interface. This is due to the fact that surfactants suppress waves and can be thought of as a rigid interface.

For a number of scientific and industrial applications, it is of interest to accurately measure the flow and velocity profile of the plane Couette flow. This is a straightforward task when the flow is accessible from the side (along the $y$-axis in Figure 1). In this case the velocity can be measured at a range between the two plates and the gradient with respect to $z$ computed.

Very often, it is not possible to measure the fluid flow in this fashion, since the flow is not accessible from the side. This can either be due to the minute separation of the plates in microfluidic applications or because a very small boundary layer is modulated by relatively high waves at the air-water interface.

The velocity profile in plane Couette flow is given by Equation (3). This leads to the time dependence $x = \frac{z}{\delta}U \cdot t = \frac{z}{\mu}\tau \cdot t$ of the position of a marker attached to the flow at $t = t_0 = 0$. Here the viscous shear $\tau$ is given by $\tau = \mu/\delta U$.

It shall be assumed that the fluid elements are marked at time $t_0 = 0$ with an appropriate technique. For microfluidic applications, such a technique relies on the activation of caged dyes with a XeF Excimer laser. At the air-water interface,

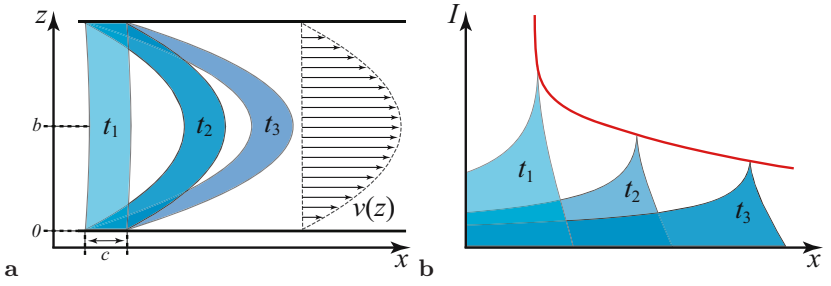


**Fig. 3.** A sketch of the intensity profile of the dye for a Poiseuille flow at three times $t_1$-$t_3$ is shown in **a** together with the velocity profile $v(z)$. The projection of these profiles onto one plate as seen by the camera is shown in **b**.

water parcels are heated up with ca $CO_2$ laser and visualize with an infrared camera. Without taking the Lambert-Beer law into consideration and thus no attenuation with depth, the marker highlights a homogeneous three dimensional structure inside the viscous boundary layer. A sketch of such a structure is presented in Figure 2**a**.

Once the structure is written at time $t_0$, it is sheared due to the velocity profile as indicated in the same figure in successive time steps $t_1 - t_4$. In the imaging process the dimension of depth $z$ is lost through integration. The projection of intensities $I$ onto the surface at $z = \delta$ is given by

$$I(x,t) = \int_{\frac{\delta\cdot(x-c)}{U\cdot t}}^{\frac{\delta\cdot x}{U\cdot t}} 1\, dz = \frac{x\cdot\delta}{t\cdot U} - \frac{(x-c)\cdot\delta}{t\cdot U} = \frac{c\cdot\delta}{t\cdot U} = \frac{\mu\cdot c}{t\cdot\tau} \tag{4}$$

Here $c$ denotes the width of the area marked, as can be seen in Figure 2.

Differentiating Equation (4) with respect to time leads to

$$\frac{dI}{dt} = \frac{d}{dt}\left(\frac{c\cdot\delta}{t\cdot U}\right) = -\frac{1}{t}I. \tag{5}$$

Estimating the velocity of the intensity structures subject to a plane Couette type shear flow with a linear velocity gradient can thus be computed by solving the differential equation $dI/dt = -(t)^{-1}I$ which can be written in an extension of the well known brightness change constraint equation (BCCE) [6] as

$$\frac{dI}{dt} = u_1\frac{\partial I}{\partial x} + u_2\frac{\partial I}{\partial y} + \frac{\partial I}{\partial t} = -\frac{1}{t}I. \tag{6}$$

Rewriting this equation in vector notation leads to

$$\frac{dI}{dt} = d^\top\cdot p = \left[\tfrac{1}{t}I\ \tfrac{\partial I}{\partial x}\ \tfrac{\partial I}{\partial y}\ \tfrac{\partial I}{\partial t}\right]\cdot\left[1\ u_1\ u_2\ 1\right]^\top = 0\ . \tag{7}$$

This equation can be thought of as the motion equation of density structures visualized through integration across a plane Couette type flow.

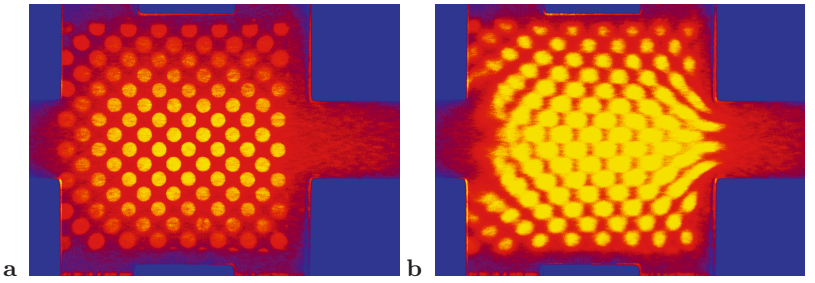


**Fig. 4.** In **a** and **b** two frames of a microfluidic image sequence are shown. The implication of Taylor dispersion can be clearly observed. Structures seem to diffuse in the direction of fluid flow [7].

### 2.2 Plane Poiseuille Flow

In Poiseuille flow, the configuration is similar to that of Couette flow. Once more, a fluid is bounded by two infinite plates separated by a distance $\delta = 2 \cdot b$. However, for Poiseuille flow both plates are stationary ($U_\delta = U_0 = U = 0$) and the flow is driven only by a pressure difference $dp/dx$. In this configuration, Equation (2) reduces to

$$u(z) = -\frac{z}{2\mu}\frac{dp}{dx}(\delta - z) = -\frac{z}{\mu}\frac{dp}{dx}\left(b - \frac{z}{2}\right) = \frac{a}{2}z^2 - a \cdot b \cdot z \quad \text{with} \quad a = \frac{1}{\mu}\frac{dp}{dx}. \tag{8}$$

This type of flow and the associated quantities are visualized in the sketch of Figure 3 **a**.

Similar to plane Couette flow as presented in Section 2.1, plane Poisseuille flow has a broad range of applications, especially in microfluidics. In these types of applications it is important to measure the velocity of fluid parcels in between parallel plates. However, due to the boundary conditions of the microfluidic devices, it is not possible to visualize the cross section of the flow. A marker such as a caged dye is introduced into the fluid and a pattern is written to the fluid at time $t = 0$. In later times, this structure is sheared by the parabolic velocity profile developed by the Poiseuille flow. The 2D cut of this process is shown for three time steps $t_1$-$t_3$ in Figure 3**a**. Through this projection, it appears as though the structure written to the fluid is smeared in the direction of the fluid flow over time. This process which might appear similarly to anisotropic diffusion, is also known as Taylor dispersion [8]. An image of this type of process can be seen in Figure 4.

The marker is visualized through one of the plates, leading to an integration of the dye with respect to depth $z$. This results in

$$I = \int_{b\pm\sqrt{b^2+\frac{2x}{at}}}^{b\pm\sqrt{b^2+\frac{2(x+c)}{at}}} 1 dz = \sqrt{b^2 + \frac{2 \cdot (c+x)}{a \cdot t}} - \sqrt{b^2 + \frac{2 \cdot x}{a \cdot t}}. \tag{9}$$

The projected intensity structure is given by Equation (9). This structure can be developed in a Taylor series around $t = 0$. This results in

$$I = \sqrt{\frac{2}{t}}\left(\sqrt{\frac{c+x}{a}} - \sqrt{\frac{x}{a}}\right) + \frac{b^2\sqrt{t}}{2\sqrt{2}}\left(\sqrt{\frac{a}{c+x}} - \sqrt{\frac{a}{x}}\right) + \mathcal{O}\left(t^{3/2}\right). \tag{10}$$

Differentiating the first term of the expansion in time leads to

$$\frac{dI}{dt} = \frac{d}{dt}\left(\sqrt{\frac{2}{t}}\left(\sqrt{\frac{c+x}{a}} - \sqrt{\frac{x}{a}}\right)\right) = -\frac{1}{2t}I. \tag{11}$$

Estimating the velocity of the intensity structures subject to Taylor dispersion can thus be computed by solving the differential

$$\frac{dI}{dt} = u_1\frac{\partial I}{\partial x} + u_2\frac{\partial I}{\partial y} + \frac{\partial I}{\partial t} = -\frac{1}{2t}I. \tag{12}$$

This linear differential equation can be rewritten in vector notation which leads to

$$\frac{dI}{dt} = d^\top \cdot p = \left[\, \tfrac{1}{2t}I \;\; \tfrac{\partial I}{\partial x} \;\; \tfrac{\partial I}{\partial y} \;\; \tfrac{\partial I}{\partial t} \,\right] \cdot \left[\, 1 \; u_1 \; u_2 \; 1 \,\right]^\top = 0. \tag{13}$$

### 2.3 *n*-th Order Velocity Profiles

For a number of fluid flow configuration, the velocity profile can be approximated to leading order by

$$u(z) = A \cdot z^n, \tag{14}$$

where A is a term independent of $z$ and $t$. The integration across the profile results in

$$I = \int_{\sqrt[n]{\frac{x-c}{A\cdot t}}}^{\sqrt[n]{\frac{x}{A\cdot t}}} 1 \,\mathrm{d}z = \sqrt[n]{\frac{x}{A\cdot t}} - \sqrt[n]{\frac{x-c}{A\cdot t}}. \tag{15}$$

Differentiating this expression with respect to time directly leads to the following differential equation

$$\frac{dI}{dt} = u_1\frac{\partial I}{\partial x} + u_2\frac{\partial I}{\partial y} + \frac{\partial I}{\partial t} = -\frac{1}{n\cdot t}I, \tag{16}$$

which can be written in vector notation giving

$$\frac{dI}{dt} = d^\top \cdot p = \left[\, \tfrac{1}{nt}I \;\; \tfrac{\partial I}{\partial x} \;\; \tfrac{\partial I}{\partial y} \;\; \tfrac{\partial I}{\partial t} \,\right] \cdot \left[\, 1 \; u_1 \; u_2 \; 1 \,\right]^\top = 0. \tag{17}$$

It is quite easy to see that this is a generalization of the previous cases of plane Couette flow ($n = 1$), compared to Equation (6) and (7) and of plane Poiseuille flow ($n = 2$), compared to Equations (12) and (13).

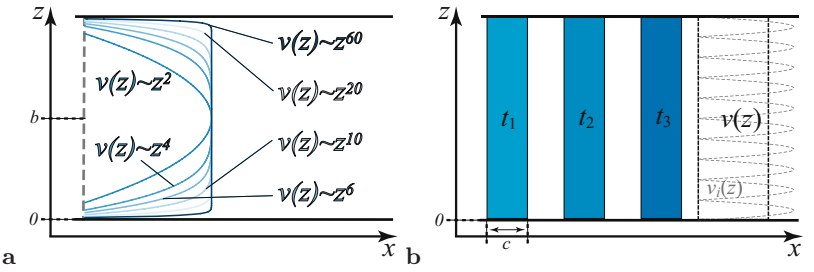


**Fig. 5.** In **a** a sketch of velocity profiles $v(z) \sim z^n$ with $n \in \{2, 4, 6, 10, 20, 60\}$. The higher the order $n$ the better the approximation of a constant profile as shown in **b**. In the xylem of plants, the flow can be approximated by a number of small hollow tubes with a Poiseuille flow in between, as shown in **b**.

The both relevant flow configuration between parallel plates discussed so far have been plane Couette flow and plane Poiseuille flow. It might seem superfluous to expand the model to $n$-th order. However, there are flows for which higher order flow profiles are relevant. In Figure 5**a** the velocity profiles for a range of higher order models is sketched. It becomes apparent, that the central part of the profile becomes increasingly flat. Choosing ever higher order up to $\lim_{n\to\infty}$, we end up with a constant velocity profile with sharp edges. Water carrying tissue in plants can be approximated by an array of Poiseuille flows as sketched in Figure 5**b**. For an increasing number of such small "'pipes"', this flow can be approximated by this $\lim_{n\to\infty}$ flow.

It is interesting to note that the motion Equations (16) and (17) reduce to

$$\frac{dI}{dt} = u_1\frac{\partial I}{\partial x} + u_2\frac{\partial I}{\partial y} + \frac{\partial I}{\partial t} = -\frac{1}{n\cdot t}I, \quad \text{and} \quad \lim_{n\to\infty} \frac{dI}{dt} = 0, \tag{18}$$

which is the standard BCCE [6]. This means that in the case of a constant velocity profile with depth, integration over depth does not matter and the standard BCCE can be used for estimating velocities of projected quantities. Intuitively this does make sense and is quite an expected behavior.

## 3 Parameter Estimation

The technique of simultaneously estimating optical flow and change of image intensity is well known in literature [9,10,11,12]. Details of the technique employed in the context of this manuscript are an extension of the structure tensor approach [13] and have been explained previously [14]. Accuracy improvements were introduced in [15] and [16].

Basically, the relevant constraint equations (7), (13) and (17) provide one constraint in two unknowns leading to an ill-posed problem. This can be solved

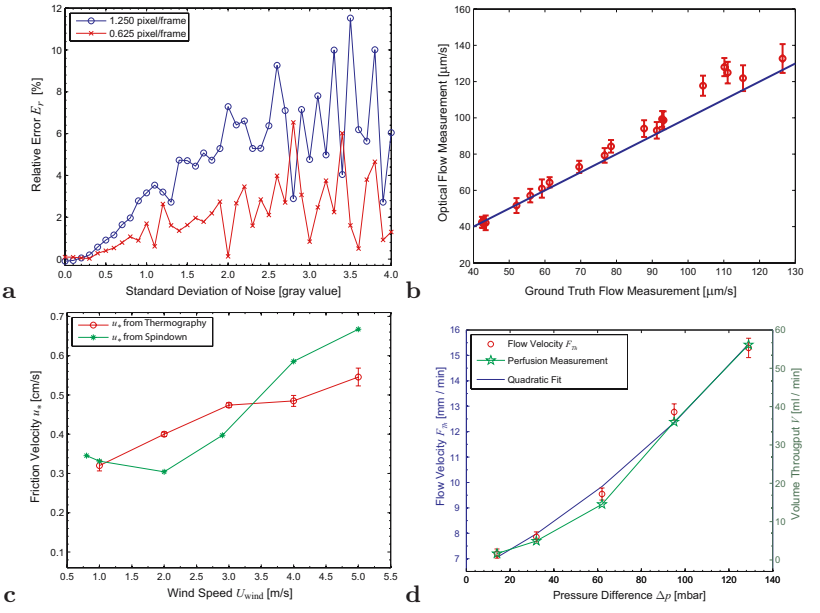


**Fig. 6. a** Relative error for Gaussian test sequences with two different velocities ($u_1 = 0.625$ pixel/frame and $u_2 = 1.25$ pixel/frame) and varying noise levels. **b** Comparison of measured values (red circles) compared to ground truth measurement (solid blue line). Error bars: deviations in three successive frames. **c** Measurements conducted in a small wind wave facility. **d** Perfusion measurements of the center vein of a ricinus leaf.

from additional constraints. A commonly made assumption is that of a locally smooth motion field. Therefore, the aforementioned constraint equations can be pooled over a local neighborhood, leading to an overdetermined system of equations. This system can be solved for the parameter $\boldsymbol{v}$ using a weighted total least squares approach [17].

## 4 Applications

In order to test the presented motion models, test measurements were performed. First, the basic applicability was tested on synthetic sequences. The injection of a tracer into Couette and Poiseuille flow was modeled and the integration was performed. The distribution of the tracer in the projection plane was modeled to be a 2D Gaussian. This test pattern was corrupted with normally distributed noise of varying standard deviation. Also different flow velocities were simulated. The results of these measurements are shown in Figure 6**a** for the case of Poiseuille flow. It should also be noted that the velocity computed is that of the center layer in between the two plates. From this center plate velocity, the full flow profile can be reconstructed.

Apart from measurements on simulated data, the technique was also tested on real world measurements with ground truth. To test the performance on microfluidic flow, a spatially homogeneous pressure driven flow was set up in a microfluidic chamber [18]. Ground truth was derived from accurate measurements of the water flow through the chamber. Results are presented in [7] and recapitulated in Figure 6**b**. The slight bias in some measurements can be attributed to calibration errors of the flow meter [7]. The data points were measured by integrating over the center part of three frames. The standard deviation was computed over the same area of the three frames. It can clearly be seen that there exists a good agreement between measurement and ground truth. For most data points, the ground truth value is well within the error bar.

At the air-water interface, measurements have been conducted by heating up patches of water with an $CO_2$ laser leading to similar patterns as in the microfluidic case. From the velocity profile of Couette flow, the shear at the interface can be computed leading to the friction velocity $u_\star$, an important parameter for parameterizing air-water interactions. This parameter has been measured with an alternative instrument for ground truth. The comparison of these measurements is presented in Figure 6**c**. These measurements have been the first time that this parameter could be measured directly [19]. The difficulty of measuring this parameter is reflected in deviations to the standard measuring technique.

Similar to the microfluidic application, ground truth measurements have been performed in a botanical applications [20]. The leaf of a ricinus plant was perfused and thus the pressure driven water flow through it was measured. A $CO_2$ laser was used for writing patterns on the leaf and these patterns were visualized with an infrared camera. The velocity of these structures were measured and compared to the perfusion measurements. The results showing excellent agreement are presented in Figure 6**d** for different flow velocities [20].

## 5 Conclusion

In this contribution, motion models were presented incorporating brightness changes due to the integration of a tracer across velocity profiles. These models connect the motion of an object in the scene with gray value changes in the acquired image sequences. This brightness change is very similar in appearance to anisotropic diffusion. Expressions for first- and second-order flow profile have been developed as well as general $n$-th order profiles. Applications of these models were presented, including shear flow at the air-water interface, Poiseuille flow in pressure driven microfluidic applications and an $n$-th order model in an botanical application. The validity of the presented motion models was tested on simulations as well as on ground truth image sequences. The parameters of these motion models were estimated in a local structure tensor approach. Only through this approach is the accurate estimation of fluid flow possible. This made the presented applications feasible for the first time. This framework can be readily extended to incorporate physically based regularization to increase accuracy of the results further.

## References


1. Corpetti, T., Etienne, M., Perez, P.: Dense estimation of fluid flows. IEEE PAMI 24(3) (March 2002)
2. Ruhnau, P., Kohlberger, T., Nobach, H., Schnörr, C.: Variational optical flow estimation for particle image velocimetry. Exp. in Fluids 38, 21–32 (2005)
3. Ruhnau, P., Schnörr, C.: Optical stokes flow: An imaging based control approach. Exp. in Fluids 42, 61–78 (2007)
4. Taylor, J.A., Yeung, E.S.: Imaging of hydrodynamic and electrokinetic flow profiles in capillaries. Anal. Chem. 65(20), 2928–2932 (1993)
5. Kundu, P.K.: Fluid Mechanics. Academic Press, London (1990)
6. Haußecker, H., Spies, H.: Motion. In: Jähne, B., Haußecker, H., Geißler, P. (eds.) Handbook of Computer Vision and Applications, vol. 2, Academic Press, London (1999)
7. Garbe, C.S., Roetmann, K., Beushausen, V., Jähne, B.: An optical flow mtv based technique for measuring microfluidic flow in the presence of diffusion and taylor dispersion. Exp. in Fluids (accepted, 2007)
8. Taylor, G.: Conditions under which dispersion of a solute in a stream of solvent can be used to measure molecular diffusion. Proc. Royal Soc. London Ser. A 225, 473–477 (1954)
9. Negahdaripour, S., Yu, C.H.: A generalized brightness chane model for computing optical flow. In: ICCV, Berlin, pp. 2–7 (1993)
10. Zhang, D., Herbert, M.: Harmonic maps and their applications in surface matching. In: CVPR'99, June 1999, Fort Collins, Colorado (1999)
11. Haußecker, H., Garbe, C., Spies, H., Jähne, B.: A total least squares framework for low-level analysis of dynamic scenes and processes. In: DAGM, Bonn, Germany, pp. 240–249. Springer, Heidelberg (1999)
12. Haußecker, H., Fleet, D.J.: Computing optical flow with physical models of brightness variation. IEEE PAMI 23(6), 661–673 (2001)
13. Bigün, J., Granlund, G.H., Wiklund, J.: Multidimensional orientation estimation with application to texture analysis and optical flow. IEEE PAMI 13(8), 775–790 (1991)
14. Garbe, C.S., Spies, H., Jähne, B.: Estimation of surface flow and net heat flux from infrared image sequences. J. of Math. Im. and Vis. 19(3), 159–174 (2003)
15. Garbe, C.S., Jähne, B.: Reliable estimates of the sea surface heat flux from image sequences. In: Radig, B., Florczyk, S. (eds.) Pattern Recognition. LNCS, vol. 2191, pp. 194–201. Springer, Heidelberg (2001)
16. Garbe, C.S., Spies, H., Jähne, B.: Mixed ols-tls for the estimation of dynamic processes with a linear source term. In: Van Gool, L. (ed.) Pattern Recognition. LNCS, vol. 2449, pp. 463–471. Springer, Heidelberg (2002)
17. Van Huffel, S., Vandewalle, J.: The Total Least Squares Problem: Computational Aspects and Analysis. In: SIAM, Philadelphia (1991)
18. Roetmann, K., Schmunk, W., Garbe, C.S., Beushausen, V.: Micro-flow analysis by molecular tagging velocimetry and planar raman-scattering. Exp. in Fluids (accepted, 2007)
19. Garbe, C.S., Degreif, K., Jähne, B.: Estimating the viscous shear stress at the water surface from active thermography. In: Garbe, C.S., Handler, R.A., Jähne, B. (eds.) Transport at the Air Sea Interface, pp. 223–239 (2007)
20. Garbe, C.S., Pieruschka, R., Schurr, U.: Thermographic measurements of xylem flow in plant leaves. New Phytologist (in preparation) (2007)